Behaviour of hybrid inside/out Janus nanotubes at an oil/water interface. A route to self-assembled nanofluidics?

P. Picot, O. Taché, F. Malloggi, T. Coradin, A. Thill

Faraday Discussions

Cite this: *Faraday Discuss.*, 2016, **191**, 391

PAPER

Behaviour of hybrid inside/out Janus nanotubes at an oil/water interface. A route to self-assembled nanofluidics?†

P. Picot,[a] O. Taché,[a] F. Malloggi,[a] T. Coradin[b] and A. Thill*[a]

Received 1st March 2016, Accepted 12th April 2016
DOI: 10.1039/c6fd00034g

Imogolites are natural aluminosilicate nanotubes that have a diameter of a few nanometers and can be several microns long. These nanotubes have different chemical groups on their internal (Si–OH) and external (Al–OH–Al) surfaces, that can be easily functionalised independently on both surfaces. Here we show that taking advantage of the particular shape and chemistry of imogolite, it is possible to prepare inside/out Janus nanotubes. Two kinds of symmetric Janus nanotubes are prepared: one with an external hydrophilic surface and an internal hydrophobic cavity (imo-CH_3) and one with an external hydrophobic surface and a hydrophilic internal cavity (OPA-imo). The behaviour of such inside/out Janus nanotubes at oil/water interfaces is studied. The OPA-imo adsorbs strongly at the oil/water interface and is very efficient in stabilising water-in-oil emulsions through an arrested coalescence mechanism. Imo-CH_3 also adsorbs at the oil/water interface. It stabilises oil-in-water emulsions by inducing slow oil-triggered modifications of the viscosity of the continuous phase. The possible transport of small molecules inside the imo-CH_3 nanotubes is evidenced, opening up routes towards self-assembled nanofluidics.

Introduction

Pickering emulsions are oil-in-water (O/W) or water-in-oil (W/O) dispersions stabilised by solid particles.[1] The stabilisation is due to the preferential adsorption of particles at the interface between two immiscible liquids. Such adsorption occurs for homogeneous particles when they are partially wetted by both fluids.[2] In this case, the contact angle controls the positioning of the particles at the interfacial layer. Homogeneous functionalisations are generally performed in order to control this contact angle and therefore the structure of the interfacial layer.[3] Another strategy enabling tuning the behaviour of particles at an oil/water

[a]*LIONS, NIMBE, CEA, CNRS, Université Paris-Saclay, 91191 Gif sur Yvette, France. E-mail: antoine.thill@cea.fr*
[b]*Sorbonne Universités, UPMC Univ. Paris 6, CNRS, Collège de France, LCMCP, Paris, France*
† Electronic supplementary information (ESI) available. See DOI: 10.1039/c6fd00034g

interface is to use inhomogeneous (or asymmetric) surfaces. The association of two surfaces with different wettability on a single particle gives the so-called Janus particles. For example, a spherical particle with hydrophilic and hydrophobic hemispheres will strongly adsorb at an oil/water interface and efficiently stabilises Pickering emulsions.[4] The positioning of the particle at the interface is then defined by the extent of the different surfaces. Many methods have been developed to produce large quantities of Janus nanoparticles with various shapes like sheets, ribbons or rods.[5] However, there are only very few examples of Janus nanotubes used for Pickering emulsions. Stabilisation of emulsions using polymer grafting on multi-wall carbon nanotubes was achieved but the "nanotubular" (*i.e.* the existence of both an internal and an external surface) nature of the particles was not evidenced to be a key parameter in the stabilisation process.[6,7] Using nanotubular clay, Janus nanotubes are also prepared and used to stabilise emulsions but, here again, the importance of the tubular shapes was not clearly identified.[8]

In this work, we wanted to use a system where the nanotubular morphology of the nanoparticles plays a crucial role in the behaviour of the particles at an oil/water interface. Among inorganic nanotubes, aluminosilicates are particularly attractive because of the wide availability and low cost of their constitutive elements. Imogolite is an example of aluminosilicate nanotube whose synthesis is relatively easy. Interestingly, imogolites have been discovered well before carbon nanotubes in 1962 by Yoshinaga and Aomine.[9] Synthetic imogolites exist in a form mimicking natural nanotubes with an average composition of $(OH)_3Al_2O_3Si(OH)$. The diameter of synthetic imogolites is monodisperse and can be tuned depending on the synthesis conditions from 2 to 2.8 nm.[10,11] They are formed thanks to the curving of a gibbsite layer. The bonding of silicon tetrahedron *via* three Al–O–Si bonds is one of the main reasons explaining their well-defined curvature (Scheme 1). In recent years, it has been realised that many structural and chemical modifications of imogolite-like structures can be achieved. It is possible to (i) replace Si by Ge,[12] (ii) vary the morphology from nanospheres to nanotubes,[13] (iii) control the formation of single wall or double wall nanotubes,[14,15] (iv) control the diameter of the nanotubes,[11] (v) modify their external surface through chemical grafting,[16] (vi) modify the wall composition *via* incorporation of iron atoms up to 1%,[17,18] and (vii) modify the internal surface through post functionalisation or directly during the synthesis.[19,20] These latter modifications are possible because, in contrast to CNT, imogolite nanotubes are naturally open at both ends and their growth mechanism does not involve the use of any catalytic processes which could lead to unwanted clogging of the cavity.

All the advantages mentioned above make imogolite-derived nanoparticles a whole family of nanobuilding blocks. Most of them are probably not yet discovered and their potential applications are largely unexplored.[21] Among possible modifications, some lead to the formation of what we will call hereafter inside/out Janus nanotubes. Indeed, the grafting of alkyl-phosphonic acids onto the external surface of imogolite nanotubes gives a hydrophobic external surface while the internal surface remains hydrophilic (Scheme 1).[22] The reverse is possible when using triethoxymethylsilane as a chemical precursor leading to nanotubes having a hydrophobic internal cavity covered by $Si–CH_3$ groups and a hydrophilic external surface providing colloidal stability in water (Scheme 1).[19]

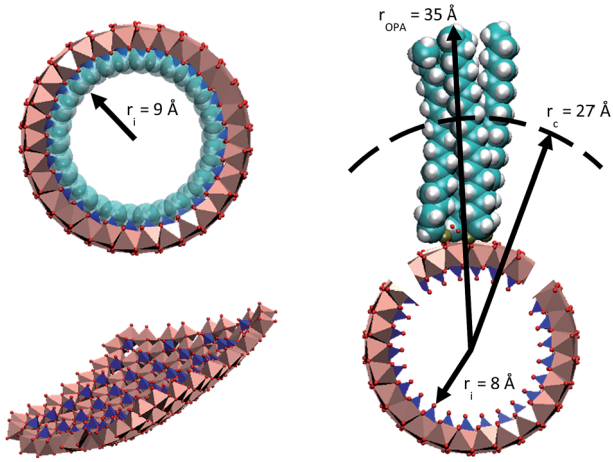

Scheme 1 Side view of imo-CH_3 (top left), proto-imogolite (bottom left), portion of bare imogolite (bottom right) and OPA-imo (top right). Light blue and white spheres are respectively carbon and hydrogen atoms of the methyl groups (hollows for imo-CH_3 and filled for OPA-imo), red and brown spheres are oxygen and phosphorous atoms respectively. Pink octahedra and blue tetrahedra are, respectively, aluminium octahedra and silicon tetrahedra. For clarity, only a few OPA molecules are represented and hydrogen of imogolites hydroxyl groups are omitted. r_i, r_{OPA} and r_c are respectively the radii of the internal cavity, and of OPA-imo without and with inter-penetration of alky chains.

In this work, we hypothesised that such inside/out Janus nanotubes could exhibit very interesting properties and especially that their nanotubular nature can be fully involved in the control of their behaviour at oil/water interfaces. Here, the modification of both the external and internal surfaces of imogolites is described, producing nanotubes with shape and chemical anisotropy. Their adsorption at an oil/water interface and its influence on emulsion stability are studied.

Methods

Synthesis of imogolite nanotubes and hybrid nanotubes

Imogolite nanotubes are obtained through the controlled hydrolysis of a mixture of aluminium and silicon precursors. An acidic solution of aluminium is obtained by dissolving 2 mM $AlCl_3 \cdot 6H_2O$ in water. Tetraethoxysilane is added under vigorous stirring and the obtained solution is stirred for 30 min at room temperature (RT). Then, a 0.1 M sodium hydroxide solution is added at a rate of 0.1 mL min^{-1} until an OH/Al ratio of 2 is obtained. The solution is further stirred until it becomes clear. It is then kept in a close recipient at 90 °C for 5 days. After this heating period, the solution is allowed to cool to RT and concentrated by a custom ultrafiltration system (Polymem, Toulouse, France) using a 10 kDa per-sulfone membrane. The concentrated solution is dialysed against MilliQ water using an 8 kDa membrane until the conductivity of the permeate reaches 2 μS cm^{-1} or less. The final dispersion of bare imogolite, with both internal and external hydrophilic surfaces, is transparent and birefringent.

The preparation of imogolites with a hydrophobic cavity (imo-CH_3) is performed using a protocol adapted from Bottero *et al.*[19] Briefly, aluminium-*sec*-butoxide is added to a HCl solution (75 mM) in the presence of trimethoxymethylsilane (TMMS) with Al : HCl : Si molar ratios of 2 : 2 : 1. The solution is vigorously stirred at ambient temperature for an hour. After this initial mixing period, the clear dispersion is kept in an oven for 5 days at 90 °C. The solution is then allowed to cool to RT and is concentrated using tangential ultrafiltration. The resulting concentrate is centrifuged at 9000 *g* for 1.5 hours to remove a small proportion of aluminium oxides. The supernatant is a clear, viscous and birefringent dispersion that is further purified by dialysis against milliQ water until the conductivity of the permeate reaches 2 μS cm^{-1} or less.

The external surface of bare imogolite nanotubes is modified by octadecylphosphonic acid (OPA) (Scheme 1). For this, 10 mL of concentrated imogolite dispersion is added dropwise under vigorous stirring into 100 mL of absolute ethanol. Then 100 mL of ethanol with OPA is added until an imogolite : OPA molar ratio of 1 : 5 is reached. The obtained dispersion is sonicated and then stirred for 24 hours at RT. The product is then washed 5 times by centrifugation with ethanol and finally transferred into toluene.

The modified imogolite are characterised by Small Angle X-ray Scattering (SAXS) in toluene (OPA-imo) or water (imo-CH_3). Additionally, the dispersions are dried and the resulting powders are analysed by Fourier Transform Infrared spectroscopy (FTIR) in KBr. The content of organic matter is assessed by Thermogravimetric Analysis (TGA) using a heating rate of 10 °C min^{-1} and a maximum temperature of 1000 °C under N_2.

Preparation of Pickering emulsions stabilised by inside/out Janus nanotubes

OPA-imo in toluene are mixed with water for 2 min at 11 000 rpm using an UltraTurax model IKA T10 basic rod model 10N-8G. Two parameters are systematically varied: the oil/water volume ratio and the concentration of OPA-imo. The emulsions are left to stand overnight before measuring the volume of emulsified phase and the diameter of the droplets. A similar protocol is used for imo-CH_3 nanotubes except that imo-CH_3 dispersed in water are mixed with hexane. As for the previous system, the oil/water volume ratio, the time before stirring as well as the concentration of imo-CH_3 are varied.

Fourier transform infrared spectroscopy

Infrared (IR) spectra are recorded using a Bruker Vertex 70 FTIR spectrometer at RT. About 1.5 mg of dry sample powder is mixed with 130 mg of KBr powder and then pressed into an IR transparent disk. 200 scans with a resolution of 4 cm^{-1} are averaged between 400 cm^{-1} and 4000 cm^{-1}.

Small angle X-ray scattering (SAXS)

SAXS experiments are carried out using a rotating anode generator (Mo Kα = 0.711 Å) collimated by a multilayer optics and hybrid crystal slits, providing a monochromatic beam of 1×1 mm^2 at the sample position with a total incident flux of 2×10^7 photons per s. A vacuum chamber behind the sample allows minimisation of the X-ray scattering signal from air. A MAR research X-ray sensitive imaging plate detector with a pixel size of 100 μm is placed after the

output window of the vacuum chamber at a distance of 725 mm from the sample. Dispersions are filled in Kapton capillaries with a diameter of 0.24 cm. The typical counting time per sample is 3 h. Scattered intensity as a function of the wave-vector modulus $\boldsymbol{Q}$ is obtained by angular integration over the two-dimensional scattering pattern. $\boldsymbol{Q}$ is defined as $\boldsymbol{Q} = |\boldsymbol{k}_d - \boldsymbol{k}_i|$ ($\boldsymbol{k}_d$ and $\boldsymbol{k}_i$ are the wave-vectors of the scattered and incident beams, respectively) and is equal to $4\pi \sin \theta/\lambda$, where λ is the incident wavelength and 2θ is the scattering angle. Data are corrected for water, Kapton scattering and for electronic background.

TGA measurements

TGA spectra are recorded using a TGA Q50 device using a 10 °C min^{-1} temperature increase rate up to 1000 °C under nitrogen.

Viscosity measurements

Viscosity is recorded using an Anton Paar Lovis 2000 M/ME microviscometer. Measurements are made with 1.59 mm capillary, a 1.5 mm diameter steel ball, with the angle varied from 50° to 80°. We prepared three identical dispersions of imo-CH_3 in contact with hexane. A single measurement is performed on each sample to minimise disturbances due to the sample preparation. The dispersion is taken just below the hexane/imo-CH_3 interface.

Atomic force microscopy measurements

The nanotube lengths are measured using Atomic Force Microscopy (AFM, Digital Instruments, Nanoscope V). AFM characterisation is employed in tapping mode to image imogolites adsorbed on mica sheets. To obtain a homogenous deposition, 20 μL of the solutions are deposited on freshly cleaved mica (yielding a smooth negatively charged surface). Positively charged nanotubes irreversibly adsorb on the surface. Mica sheets are dried at RT over 2 days before AFM measurements.

Results

Nanotubes characterisation

The synthesised nanotubes were characterised by IR, SAXS, AFM and TGA. Fig. 1 shows the IR spectra of bare imogolite, imo-CH_3, OPA-imo and OPA. The absorption bands at 417, 552 and 690 cm^{-1} and the doublet at 935 and 977 cm^{-1} are characteristic of imogolite with a tubular structure.[23,24] Concerning imo-CH_3 the two peaks at 1275 and 781 cm^{-1} attributed to the bending of Si–CH_3 and Si–C, respectively, confirm the presence of methyl groups bound to the nanotubes.[25] Furthermore, additional peaks at 2974 and 2921 cm^{-1} corresponding to asymmetric and symmetric stretching of methyl group corroborate the presence of methyl groups for imo-CH_3 nanotubes. In addition, the imo-CH_3 nanotubes are easily dispersed in water but not in toluene, indicating that methyl groups are not located on the outside of the nanotubes but inside the cavity, in agreement with the literature.[17] In parallel, the comparison of the IR spectra of OPA-imo and OPA confirm successful grafting by the presence of CH_2 symmetric and asymmetric stretching at 2850 and 2918 cm^{-1}, the vibration at 1468 cm^{-1} and P–C vibration at 721 cm^{-1} in addition to the imogolite bands.[22,26] Such OPA-imo samples are easily

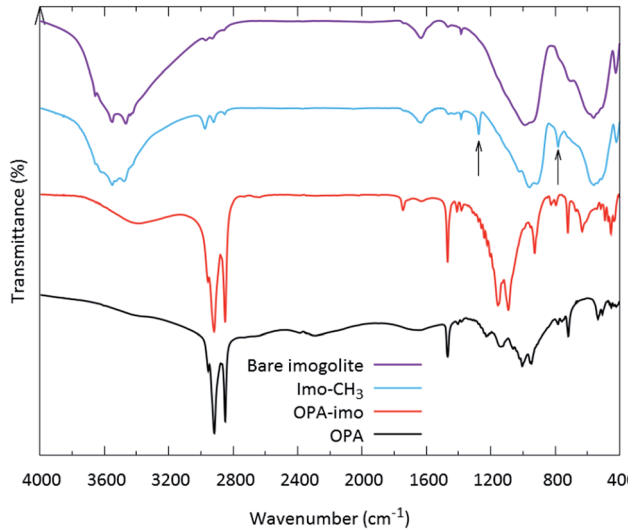

Fig. 1 FTIR spectra of bare imogolite, imo-CH_3, OPA-imo and OPA. The two arrows at 1275 and 781 cm^{-1} are attributed, respectively, to the bending of Si–CH_3 and Si–C for the imo-CH_3 curve.

dispersed in toluene but not in water, indicating that the hydrophobic moieties are present on the external surface of the nanotubes.

The TGA analyses of the bare imogolite, OPA and OPA-imo are shown in Fig. S1 in ESI† and could be used to determine the efficiency of the grafting (details of calculation are given in ESI†). The obtained mass ratio is 1.79 g OPA per g of imogolite and corresponds to 1.05 OPA molecules per imogolite structural unit. The same coverage is obtained, when computed using the same hypothesis, from the measurements of Bac *et al.* on OPA grafted AlGe imogolite.[22] This value has to be compared to the maximum coverage of 2 moles of OPA per mole of imogolite for a complete bi-dentate grafting and 1 mole of OPA per mole of imogolite for a tri-dentate grafting.

SAXS curves of OPA-imo, imo-CH_3 and bare-imo with their respective models are presented in Fig. S2.† These analyses provide information about the radius, the number of structural units per circumference, the concentration and internal electronic density of the nanotubes. The fit parameters, considering hollow cylinders and assuming a homogenous scattering length density, are presented in Table 1. It should be noted that for bare imogolite the internal electronic density is equal to the bulk water electronic density (0.33 $e^- Å^{-3}$), *i.e.* the nanotubes are full of water. For imo-CH_3, it is one third of the water value (0.11 $e^- Å^{-3}$) indicating that the nanotubes are not filled with bulk water. Although the precise physical state of water inside imo-CH_3 is difficult to determine at this time, previous studies have shown that low-density and even vapour-phase water may exist in such confined hydrophobic environments.[27] However, the sole SAXS analysis does not allow to identify the nature of the internal solvent. Noticeably, concentrations obtained from SAXS are confirmed by dry mass measurements (4.35 g L^{-1} for bare imogolite and 14.34 g L^{-1} for imo-CH_3).

Table 1 Fit parameters of bare imogolite and imo-CH_3 SAXS curves. r_i is the radius of the internal cavity, N the number of structural units per circumference, T the period of the repeat distance along the tube axis and C the concentration

Fit parameter	Bare imogolite	Imo-CH_3
r_i/nm	0.8	0.9
N	13	15
Wall thickness/nm	0.6	0.6
T/nm	0.85	0.85
Internal electronic density/e^- Å^{-3}	0.33	0.11
C/g L^{-1}	4.35	13.72
Electronic density of the wall/e^- Å^{-3}	0.7	0.7

In contrast, OPA-imo nanotubes are not perfectly dispersed and the resulting unstable dispersions do not allow a quantitative concentration measurement by SAXS. According to dry mass determination, the concentration for OPA-imo is 2.56 g L^{-1}. The SAXS curve of OPA-imo (Fig. S2†) reveals that the nanotubes form organised bundles. Considering a bi-dimensional hexagonal phase, the lattice parameter is 5.4 nm. This value is close to the one obtained by Park *et al.* (5.1 nm) and smaller than the diameter of isolated OPA-imo (7.1 nm, Scheme 1), suggesting that the alkyl chains of neighbour nanotubes can interpenetrate.[28]

Since length variation above 100 nm would modify the scattering curves mainly below the low angle limit of our SAXS apparatus, the scattered intensity could not provide reliable information on nanotube length. We have therefore used AFM to image imogolite deposited on freshly cleaved mica sheets. The concentration of the deposited dispersion was tuned to have a sub-monolayer of nanotubes. Analysing longitudinal height sections of the deposited nanotube allowed deduction of their length. Fig. 2 shows the obtained images and histograms of the average length that compile the analysis of 1100 nanotubes. It should be noted that, on these histograms, only nanotubes with a length above 100 nm are reported. The length histogram of bare imogolite (Fig. 2A) has a typical asymmetric shape with a significant number of nanotubes longer than 1.5 μm. As previously mentioned, nanotubes with a length inferior to 100 nm are not reported, although the number concentration of these smaller objects can be estimated to be more than 90% on the mica when 1 μm × 1 μm images are analysed. This is because the AFM resolution does not allow to determine accurately their length distribution. This observation is in agreement with SAXS results (Fig. S2†) showing a damping of the nanotube form factor. It suggests that the sample contains a significant proportion of proto-imogolite (Scheme 1). Proto-imogolites are "tills" and correspond to the first nanoblocks which, by assembling with another or by curving, lead to the formation of imogolite. Therefore the average length of the particles in the bare imogolite dispersion can be estimated to be below 100 nm. The length of the imo-CH_3 nanotubes could be measured with the same method. The length histogram is shown on Fig. 2B indicating an average length of 378 nm. In contrast, it was not possible to obtain a sub-monolayer of OPA-imo on mica due to the poor dispersion and low adherence on the surface. However, whereas the grafting reaction itself should not impact on

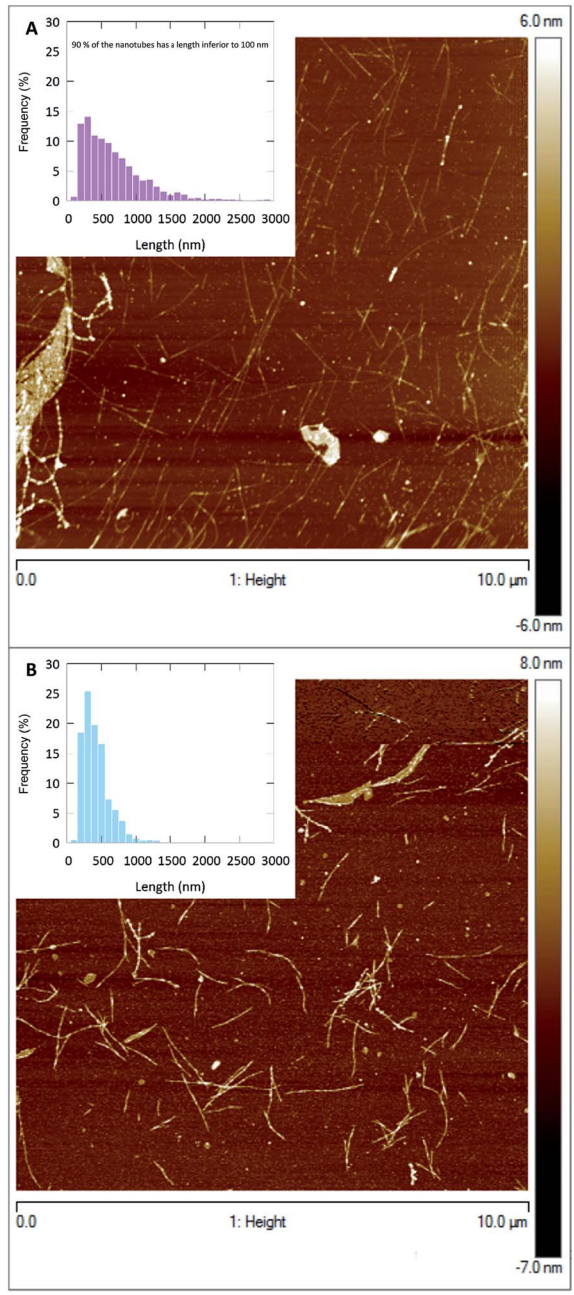

Fig. 2 AFM images and length distribution of bare imogolite (A) and imo-CH_3 (B). Only nanotubes with a length superior to 100 nm are reported on both histograms. For bare imogolite, 90% of the nanotubes has a length inferior to 100 nm.

the nanotube length, the overall procedure that involves many centrifugation and redispersion steps most probably decreases the proportion of smaller objects in the dispersion.

Pickering emulsions with Janus nanotubes

Fig. 3 shows photos of the emulsions prepared with various oil/water ratios and OPA-imo concentrations, taken one day after stirring. Stable water-in-toluene emulsions are obtained for $\Phi_w \leq 0.5$. For $\Phi_w > 0.5$, the stability of the droplets is quickly compromised and no emulsion is observed for the highest water content. The radius of the water droplets decreases when the concentration of OPA-imo increases and/or when Φ_w decreases. When left undisturbed, these emulsions are stable for months. For comparison, emulsions prepared with bare imogolite are presented in Fig. S3.† A marginal stability of the droplets is observed and attributed to the hydrophobicity of the (Al–OH–Al) surface.[29]

In the case of experiments with a dispersion of imo-CH_3 in contact with hexane, no stable emulsion is observed one day after stirring. However, when the imo-CH_3 dispersion has been in contact with hexane for one week before stirring, an emulsion is obtained that remains stable over one week (Fig. 4). Noticeably, during the one-week ageing period, the viscosity of the imo-CH_3 dispersion (and therefore of the emulsion continuous phase) has increased compared to its initial value.

Therefore, OPA-grafted imogolite can stabilise W/O, but not O/W, Pickering emulsions very efficiently. It seems that the droplet size is controlled by an arrested coalescence mechanism. In the case of imo-CH_3, the stability of the emulsions is more complex and apparently linked to the viscosity of the continuous phase. These two mechanisms are discussed in more detail in the following sections.

Discussion

OPA-imo: arrested coalescence by anisotropic particles

From an energetic perspective, the driving force towards particle adsorption at the oil/water interface is due to the gain of interfacial energy between oil and the

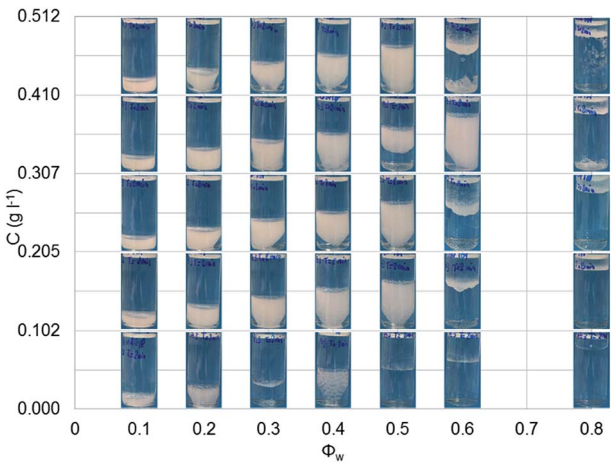

Fig. 3 Emulsion test with OPA-imo, toluene and water. C corresponds to the concentration of OPA-imo in the total volume.

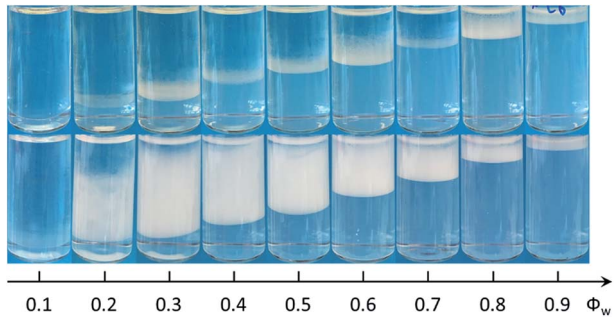

Fig. 4 Emulsion test with hexane and imo-CH_3. Top line: samples is stirred just after preparation; and bottom line: one week after preparation. Photos taken one week after stirring.

water trapped inside OPA-imo tubes. Indeed, the perpendicular position of OPA-imo at the interface with one end of the nanotube in contact with the oil/water interface is the only possibility to minimise this unfavourable contact between the hydrophilic nanotube ends and oil. Considering the diameter of the nanotube ($d = 1.6$ nm) and the toluene/water interfacial tension ($\sigma = 36.1$ mN m^{-1}) the gain in energy upon adsorption is of the order of $E_a = \sigma d^2\pi/2 = 27$ kT.[30] Moreover, in the case of OPA-imo, there is probably also an inter-particle favourable attraction due to the combination of van der Waals attraction and osmotic pressure associated with interpenetration of the grafted OPA chains. The quantification of this attractive energy goes beyond the scope of this work but a rough estimate of a few kT nm^{-1} would be reasonable.[31] Therefore, we can expect a total gain in energy for the OPA-imo nanotube of at least 100 kT making adsorption a probably irreversible process. When particles irreversibly adsorb at the oil/water interface, it is classically observed in Pickering emulsions that the increase of adsorbed particles controls the size of the droplets through an arrested coalescence mechanism.[32,33]

From a structural point of view, there are two extreme options for the adsorption of nanotubes at the oil/water interface: perpendicular or parallel to the interface. When the adsorbed particles are highly anisotropic, these two adsorption modes lead to full coverage of the droplet surface at very different concentrations. Indeed, for an adsorption parallel to the interface, the surface coverage is given by (eqn (1)):

$$\delta_{par} = \frac{NDL}{S_d} \quad (1)$$

where N is the number of adsorbed nanotubes, D and L are the respective diameter and length of the adsorbed nanotubes, and S_d is the total surface of the droplets. The number of adsorbed nanotubes is given by $N = C_m N_{avo} TV/(ML)$ with C_m the mass concentration of adsorbed nanotubes, M the molar mass per repeat period T along the nanotube axis, V the volume of grafted imogolite added, and L the length of the nanotube. The total surface of the droplets is given by $S_d = 3V_d/R_d$ where V_d is the volume of the dispersed phase and R_d the average radius of the droplets. Combining these expressions, it follows that the droplet diameter obtained through an arrested coalescence mechanism will follow (eqn (2)):

$$R_d \sim \frac{V_d}{D C_m V} \quad (2)$$

If we now assume that the nanotubes adsorb in a perpendicular configuration, then the surface coverage is given by (eqn (3)):

$$\delta_{perp} = \frac{N \pi D^2}{4\ S_d} \quad (3)$$

Using the same expressions for N and S_d in this equation, we can show that the arrested coalescence will give a droplet radius with (eqn (4)):

$$R_d \sim \frac{V_d L}{D^2 C_m V} \quad (4)$$

It is easy to understand that in the case of the parallel adsorption the arrested coalescence does not depend on the nanotube length (*i.e.* R_d is independent of L in eqn (2)). For instance, if all adsorbed nanotubes are cut in half, the same surface will be occupied at the interface. On the contrary, in the case of perpendicular adsorption at the interface, length matters. If the nanotubes are cut in their middle, the new nanotubes, not attached to the interface, can stabilise the same interfacial area. Finally, twice the surface can be covered for the same mass of nanotubes when their length is divided by two. The ratio of droplet size at arrested coalescence in the two extreme configurations is given by $4L/(\pi D)$, which is close to 100 in the case of imogolite. Therefore, measuring the average size of the droplets as a function of the OPA-imo concentration should give some clues to conclude on the adsorption geometry. Fig. 5 shows the evolution of the experimentally measured droplet radius (software imageJ analysis) as a function of the

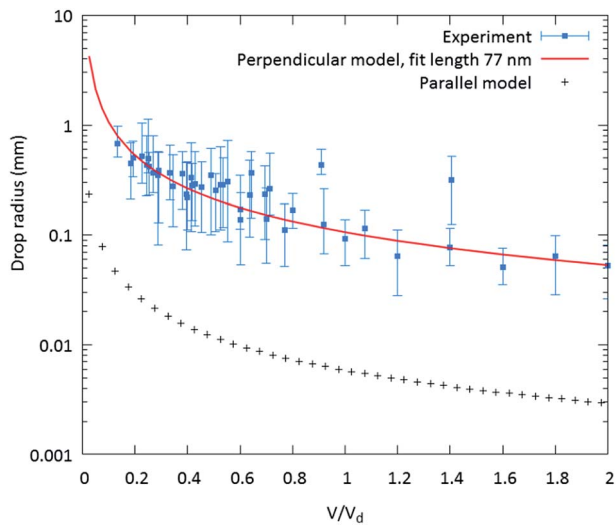

Fig. 5 Evolution of the drop radius *versus* ratio V/V_d for experiment, the perpendicular model with a fit length of 77 nm and the parallel model.

ratio V/V_d, where V_d corresponds to the volume of emulsified water. In the same Figure, the theoretical radii given for the two extreme adsorption scenarios are reported. First of all, we can notice the gap of almost two orders of magnitude in the droplet radius values between the parallel and perpendicular model. Clearly, the experimental values fit very well the perpendicular adsorption model, in agreement with the above-discussed energetic considerations. Second, the fact that the best fit for the perpendicular model is obtained for an average tube length inferior to 100 nm indicates that these smallest OPA-imo contribute to the stabilisation of the emulsion.

Imo-CH_3: gel formation, viscosity effects and transport properties

Imo-CH_3 nanotubes are prepared in water and do not initially contain oil in their cavity. However, it is known that they can capture small hydrophobic molecules.[34] In order to follow this process, Nile Red dye was selected as a probe and added to the oil phase.[35] Fig. 6 shows photos of the Nile-Red-in-hexane solution in contact with water and with an imo-CH_3 dispersion just after preparation for pictures (a) and (b) and after three days of stirring for pictures (c) and (d). The water phase on images (a) and (c) remains colourless. In the presence of imo-CH_3, a pink colour is first observed at the oil/water interface (b) and then the water phase turns pink/violet whereas the oil phase is colourless. This can be explained considering that the hydrophobic inner cavity of imo-CH_3 is able to be filled with the oil phase, also extracting the dye. When the dye is initially confined within the nanotubes located at the oil/water interface, it can then be transferred to the imo-CH_3 particles present in the bulk water phase, resulting in its full coloration after 3 days.

Such filling should provide a driving force toward nanotube adsorption at the oil/water interface. Considering a diameter of 1.8 nm and an interfacial tension between water and hexane of 50 mN m^{-1}, the gain in interfacial energy upon adsorption can be estimated by $\sigma d^2\pi/2 = 49$ kT.[30] However, the imo-CH_3 nanotubes are stable in aqueous solution thanks to interparticle electrostatic repulsion. This repulsion prevents their close packing and therefore the full coverage of the oil/water interface. In this case, we can observe an equilibrium between dispersed and adsorbed nanotubes. The surface coverage can therefore be enhanced by increasing the nanotube concentration or by screening the electrostatic repulsion through an increase of the ionic strength. Notably, it is expected that the same amount of energy is gained when the nanotubes adsorb on the O/W

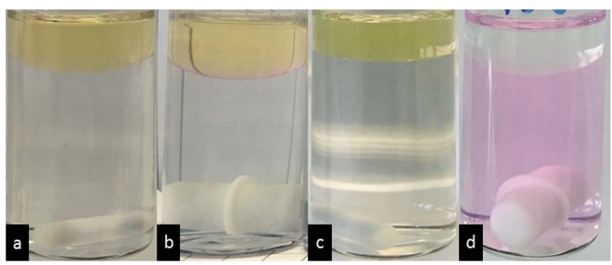

Fig. 6 Dye test: hexane/Nile Red in contact with water and hexane/Nile Red in contact with imo-CH_3 just after preparation (a) and (b) and three days after stirring (c) and (d).

interface or when the total length of the nanotubes is increased through tip–tip contacts. The presence of oil may therefore trigger an increase of the average length of the unabsorbed nanotubes. It is possible to evidence this phenomenon by following the viscosity of the imo-CH_3 dispersion in contact with oil. Fig. S4† shows that the relative viscosity of the imo-CH_3 dispersion increases from 8.79 to 12.10 after three days of contact with a hexane phase. So far, the rheological behaviour of imogolite dispersions has been sparingly studied.[36–40] Nevertheless, general laws for rod-like particles are well-known and can be tentatively used to understand the observed trends. Using the Einstein equation, for a diluted solution of particles ($\phi_v \ll 1$) the relative viscosity (defined as the ratio between the viscosity of the solution and the viscosity of the solvent, here water) is:

$$\eta_r = 1 + [\eta]\phi_v$$

With $[\eta]$ the intrinsic viscosity defined as:

$$[\eta] = \lim_{\phi \longrightarrow 0} \frac{\eta_r - 1}{\phi}$$

For uncharged, rigid and non-interacting spheres the intrinsic viscosity equals 2.5. As mentioned previously, imogolites are anisotropic particles. In this situation, the Onsager equation should be applied to calculate the intrinsic viscosity:[40,41]

$$[\eta] = \frac{4f^2}{15\ln(f)}$$

where f is the aspect ratio (ratio between the length and the diameter). Using the diameter of 3 nm given by SAXS analysis and length of 378 nm by AFM measurements, f equals 126, intrinsic viscosity equals 875 and $\eta_r = 8.72$ (for 8.79 measured). Following this equation, the increase of the relative viscosity from 8.79 to 12.1 would correspond to an increase of the aspect ratio from 126 to 154. This slow increase in viscosity is compatible with the slow nanotube growth kinetics through tip–tip collision described by Maillet *et al.*[42] When left undisturbed for very long period (about one month), imo-CH_3 dispersions in contact with oil can even form gels. This gel formation mechanism is very different from the ones induced by pH or salinity increase. In these cases, electrostatic repulsion between nanotubes is reduced up to the destabilisation of the nanotubes dispersion.

Hence, the progressive filling of the internal cavity of imo-CH_3 by the oil phase can contribute to the observed ability of nanotubes to stabilise O/W emulsion after one week of contact with hexane by two factors: favoured nanotube adsorption at the oil/water and increase of the water phase viscosity due to the growth of nanotubes. The relative contributions of the two mechanisms are difficult to establish at this time. Indeed, in this complex situation, it is not possible to assess precisely the number of adsorbed nanotubes and to determine whether perpendicular or parallel adsorption occurs. However, since the imo-CH_3 interactions with an oil-in-water interface should mirror the OPA-imo/water-in-oil situation, the former configuration is the most likely.

Conclusions

In conclusion, we report here the preparation of inside/out Janus nanotubes. Two symmetric systems are obtained: (i) external modification of bare imogolites using a phosphonic acid leads to OPA-imo with an external hydrophobic surface and a hydrophilic cavity; (ii) synthesis of imo-CH_3 leads directly to hydrophilic nanotubes with a hydrophobic cavity. These inside/out Janus nanotubes allow the stabilisation of Pickering emulsions thanks to the presence of an internal solvent. In the case of OPA-imo, the tubes are initially filled with water, their adsorption at the interface is irreversible and an arrested coalescence mechanism is observed. In contrast, the ability of imo-CH_3 to stabilise emulsions requires an aging period allowing to fill the nanotubes' interior with oil. The increase of nanotube length by tip–tip contacts resulting in the enhancement of the viscosity of the continuous phase occurs simultaneously, also favouring emulsion stability. Moreover, these nanotubes can extract a dye from an organic phase.

Structural modelling and energetic considerations suggest that the OPA-imo nanotubes adopt a perpendicular orientation at the oil/water interface. A similar organisation is expected for imo-CH_3, although the complex behaviour of these particles remains to be unravelled. Yet, the here-obtained Pickering emulsions could open the route toward self-assembled nanofluidics if two or more droplets could share connections with the same Janus nanotubes or through a network of connected Janus nanotubes.

Acknowledgements

This research has been funded by an ANR grant HIMO2 (ANR11-BS08-0002) and by the Region Ile-de-France in the framework of C'Nano IdF, the nanoscience competence center of Paris Region (HIPOP grant). The laboratory equipment for the production of imogolites is funded by a Labex NanoSaclay grant for the project PRODIGE. We want to thank Andrea Kolb for precious help and support. We also want to acknowledge the precious discussions with Elodie Bourgeat-Lami, Cécile Cottin-Bizon, Anne-Laure Biance and Christophe Ybert.

Notes and references

1 R. Aveyard, B. P. Binks and J. H. Clint, *Adv. Colloid Interface Sci.*, 2003, **100–102**, 503–546.
2 B. P. Binks and J. H. Clint, *Langmuir*, 2002, **18**, 1270–1273.
3 P. A. Kralchevsky, I. B. Ivanov, K. P. Ananthapadmanabhan and A. Lips, *Langmuir*, 2005, **21**, 50–63.
4 T. Tanaka, M. Okayama, H. Minami and M. Okubo, *Langmuir*, 2010, **26**, 11732–11736.
5 A. Walther and A. H. E. Muller, *Chem. Rev.*, 2013, **113**, 5194–5261.
6 H. Wang and E. K. Hobbie, *Langmuir*, 2003, **19**, 3091–3093.
7 N. M. Briggs, J. S. Weston, B. Li, D. Venkataramani, C. P. Aichele, J. H. Harwell and S. P. Crossley, *Langmuir*, 2015, **31**, 13077–13084.
8 C. Y. Zhou, H. Li, H. Zhou, H. Wang, P. J. Yang and S. A. Zhong, *J. Sep. Sci.*, 2015, **38**, 1365–1371.
9 N. Yoshinaga and S. Aomine, *Soil Sci. Plant Nutr.*, 1962, **8**, 22–29.

10 S. Wada, *Clays Clay Miner.*, 1987, **35**, 379–384.
11 G. I. Yucelen, D. Y. Kang, R. C. Guerrero-Ferreira, E. R. Wright, H. W. Beckham and S. Nair, *Nano Lett.*, 2012, **12**, 827–832.
12 S. Wada and K. Wada, *Clays Clay Miner.*, 1982, **30**, 123–128.
13 B. H. Bac, Y. Song, M. H. Kim, Y. B. Lee and I. M. Kang, *Chem. Commun.*, 2009, 5740–5742.
14 P. Maillet, C. Levard, E. Larquet, C. Mariet, O. Spalla, N. Menguy, A. Masion, E. Doelsch, J. Rose and A. Thill, *J. Am. Chem. Soc.*, 2010, **132**, 1208–1209.
15 A. Thill, P. Maillet, B. Guiose, O. Spalla, L. Belloni, P. Chaurand, M. Auffan, L. Olivi and J. Rose, *J. Am. Chem. Soc.*, 2012, **134**, 3780–3786.
16 W. Ma, J. Kim, H. Otsuka and A. Takahara, *Chem. Lett.*, 2011, **40**, 159–161.
17 A. Avellan, C. Levard, N. Kumar, J. Rose, L. Olivi, A. Thill, P. Chaurand, D. Borschneck and A. Masion, *RSC Adv.*, 2014, **4**, 49827–49830.
18 E. Shafia, S. Esposito, M. Armandi, M. Manzoli, E. Garrone and B. Bonelli, *Microporous Mesoporous Mater.*, 2016, **224**, 229–238.
19 I. Bottero, B. Bonelli, S. E. Ashbrook, P. A. Wright, W. Z. Zhou, M. Tagliabue, M. Armandi and E. Garrone, *Phys. Chem. Chem. Phys.*, 2011, **13**, 744–750.
20 D. Y. Kang, N. A. Brunelli, G. I. Yucelen, A. Venkatasubramanian, J. Zang, J. Leisen, P. J. Hesketh, C. W. Jones and S. Nair, *Nat. Commun.*, 2014, **5**, 9.
21 N. Arancibia-Miranda, S. Lillo and M. Escudey, *J. Chil. Chem. Soc.*, 2013, **58**, 2061–2066.
22 B. H. Bac, Y. Song, M. H. Kim, Y. B. Lee and I. M. Kang, *Inorg. Chem. Commun.*, 2009, **12**, 1045–1048.
23 V. C. Farmer, A. R. Fraser and J. M. Tait, *Geochim. Cosmochim. Acta*, 1979, **43**, 1417–1420.
24 J. L. Bishop, E. B. Rampe, D. L. Bish, Z. Abidin, L. L. Baker, N. Matsue and T. Henmi, *Clays Clay Miner.*, 2013, **61**, 57–74.
25 M. Boyer, E. Paineau, M. Bacia-Verloop and A. Thill, *Appl. Clay Sci.*, 2014, **96**, 45–49.
26 R. Luschtinetz, G. Seifert, E. Jaehne and H. J. P. Adler, *Macromol. Symp.*, 2007, **254**, 248–253.
27 S. Smirnov, I. Vlassiouk, P. Takmakov and F. Rios, *ACS Nano*, 2010, **4**, 5069–5075.
28 S. Park, Y. Lee, B. Kim, J. Lee, Y. Jeong, J. Noh, A. Takahara and D. Sohn, *Chem. Commun.*, 2007, 2917–2919.
29 B. Creton, D. Bougeard, K. S. Smirnov, J. Guilment and O. Poncelet, *Phys. Chem. Chem. Phys.*, 2008, **10**, 4879–4888.
30 J. F. Fu, B. Q. Li and Z. H. Wang, *Chem. Eng. Sci.*, 1986, **41**, 2673–2679.
31 C. L. Kitchens, M. C. McLeod and C. B. Roberts, *J. Phys. Chem. B*, 2003, **107**, 11331–11338.
32 B. P. Binks and C. P. Whitby, *Langmuir*, 2004, **20**, 1130–1137.
33 B. P. Binks, J. Philip and J. A. Rodrigues, *Langmuir*, 2005, **21**, 3296–3302.
34 M. S. Amara, E. Paineau, S. Rouziere, B. Guiose, M. E. M. Krapf, O. Tache, P. Launois and A. Thill, *Chem. Mater.*, 2015, **27**, 1488–1494.
35 P. Greenspan, E. P. Mayer and S. D. Fowler, *J. Cell Biol.*, 1985, **100**, 965–973.
36 K. Egashira, *Clay Sci.*, 1977, **5**, 87–95.
37 K. Egashira, *Clay Sci.*, 1978, **5**, 137–144.
38 K. Egashira and K. Iemura, *Soil Sci. Plant Nutr.*, 1979, **25**, 21–27.

39 Y. Tsujimoto, A. Yoshida, M. Kobayashi and Y. Adachi, *Colloids Surf., A*, 2013, **435**, 109–114.
40 N. Donkai, H. Inagaki, K. Kajiwara, H. Urakawa and M. Schmidt, *Makromol. Chem.*, 1985, **186**, 2623–2638.
41 A. M. Wierenga and A. P. Philipse, *Colloids Surf., A*, 1998, **137**, 355–372.
42 P. Maillet, C. Levard, O. Spalla, A. Masion, J. Rose and A. Thill, *Phys. Chem. Chem. Phys.*, 2011, **13**, 2682–2689.

